Vortex formation and dissolution in sheared sands

Granular Matter (2012) 14:695–705
DOI 10.1007/s10035-012-0369-5

ORIGINAL PAPER

Vortex formation and dissolution in sheared sands

Sara Abedi · Amy L. Rechenmacher · Andrés D. Orlando

Received: 8 August 2011 / Published online: 16 September 2012

Abstract Using digital image correlation, we track the displacement fluctuations within a persistent shear band in a dense sand specimen bounded by glass walls undergoing plane strain compression. The data evidences a clear, systematic, temporally recurring pattern of vortex formation, dissolution, and reformation throughout macroscopic softening and critical state regimes. During softening, locally affine deformation zones are observed at various locations along the shear band, which we argue to be kinematic signatures of semi-stable force chains. Force chain collapse then occurs, inducing vortex formation. Local jamming at the conflux of opposing displacements between adjacent vortices arrests the vortices, providing an avenue for potential new force chains to form amidst these jammed regions. The process repeats itself temporally throughout the critical state. The pattern further correlates with fluctuations in macroscopic shear stress. We characterize the nature of the observed vortices, as they are different in our sands comprised of irregular shaped particles, as compared to previous observations from experiments and numerical simulations which involved circular or rounded particles. The results provide an interesting benchmark for behavior of non-circular/non-spherical particles undergoing shear.

Keywords Sand · Vortex · Force chain · Nonaffine deformation · Meso-scale · Shear band

S. Abedi
Department of Civil and Environmental Engineering,
Massachusetts Institute of Technology,
Cambridge, MA 02139, USA

A. L. Rechenmacher (✉) · A. D. Orlando
Department of Civil and Environmental Engineering,
University of Southern California, Los Angeles, CA, USA
e-mail: arechenm@usc.edu

1 Introduction

Densely packed granular solids manifest nonaffine deformation during shear that arises largely from meso-scale particle interactions of various forms. The most widely recognized type of meso-scale nonaffine deformation arises from force chain buckling (e.g. [1–3]). In addition, vortices and "microbands" of slip deformation also have been found to yield pronounced non-affine kinematic signatures in granular material deformation. Certainly, the importance of particle rolling in sheared granular layers has been recognized (e.g. [4–6]). Moreover, Bardet and Proubet [4] found that particle rotation and macro-rotations (of the surrounding particle neighborhood) are related. This lends credence to the existence of vortex-type structures in granular shear. As vortices are by nature kinematic features, their detection and characterization requires tracking of particle motions over strain intervals commensurate with their lifetimes, which are currently not known with certainty. Vortices are thought to play a strong role in heat convection in dry granular flows [7] and in reducing the amount of frictional dissipation in fault gouges [8]. Further understanding of the behavior of these meso-scale entities, and any systematic relation between them, force chains, and microbands is crucial toward developing advanced physics-based models for these materials.

Most of our understanding about vortex structures and microbands in dense granular shear fields has been derived from numerical research using discrete element method (DEM) simulations. Williams and Rege [9,10] identified what they called "circulation cells" in sheared dense granular assemblies of circular, ellipoidal and diamond-shaped particles. Circulation cells were found to exist at all stages of deformation, and were thought to migrate, eventually coalescing within forming shear bands. Kuhn [11] in simulations of diffuse shear saw microbands of slip as a very prominent

form of deformation that were neither static nor persistent, sized only a few particles wide and long and with relatively short lifetimes. Kuhn [11] also observed circulation cells, and while a relationship between microbands and circulation cells was hypothesized, the precise nature of that relationship was thought to be complex and could not be identified. Radjai and Roux [12] in diffuse shear observed eddy-like structures to frequently appear but quickly break down, with new structures appearing in a seemingly uncorrelated fashion. Thornton and Zhang [13] and Tordesillas [14] also observed vortices and microbands to form in association with the onset of peak stress. Alonso-Marroquin et al. [8] performed simulations on circular particles and compared behavior between the extremes of fully allowing and precluding particle rolling. When particles were allowed to rotate, they observed three coexisting deformational phases: vorticity cells, rotational bearings, and slip bands. The vortex structures, however, were thought to arise only spontaneously. Tordesillas et al. [15] added the effect of rolling resistance between circular particles, and found well formed, co-rotating vortices with slip microbands between them. Buckling force chains were found through the middle of and around such vortices.

The presence of vortices in dense granular shear has also been observed experimentally. Utter and Behringer [16], in 2D Couette flow of photoelastic disks, found vortices to appear only occasionally, quickly dissipating, and were not considered to have a significant effect on long time behavior. Note, however, that this work, and most of the observations from the DEM simulations described in the paragraph above, are based on the behavior of circular or rounded particles, which are not subject to interlocking that would ostensibly be present in irregular shaped, non-circular particles such as comprising real sands. Observations about vortex formation and behavior in irregular shaped, non-circular or non-spherical particles are lacking.

Here, we present experimental evidence of the ongoing formation and dissolution of vortices in shear bands in sand undergoing plane strain compression. The sand specimens deform along glass walls, and full-field, meso-scale sand displacements are quantitatively tracked throughout shear using digital image correlation (DIC). We examine fluctuations in the displacement field throughout softening and critical state (i.e., the post-peak regime). Vortices are first seen at the softening-critical state transition, born out of the coordinated, multi-force chain buckling event seen in previous research [17,18]. The critical state, then, is characterized by an ongoing temporal pattern of: (a) grain jamming, mainly at the confluence of opposing displacements between adjacent vortices; (b) the formation of new force chains behind the jammed regions; (c) force chain collapse, inducing new vortices; (d) vortex arresting due to jamming at the confluence of opposing displacements between adjacent vortices; and so on. We highlight differences in the character of the vortices observed in our irregular, sub-rounded to sub-angular sand grains versus those obtained from previous numerical and experimental results on rounded grains. Most notably, we see very little evidence of "microbands" of slip, evidencing the strong role particle interlocking among angular to semi-angular grains has on granular behavior.

2 Experimental methods

2.1 Plane strain testing

Dense sand specimens were subjected to drained, plane strain compression. The test configuration is schematically shown in Fig. 1. A nominally 14 cm tall by 4 cm wide by 8 cm deep sand specimen is sealed inside a 0.35-mm thick, pliable latex membrane. The zero-strain condition is enforced by glass-lined acrylic walls. The membrane/glass wall surface is lubricated with clear silicon oil to minimize boundary friction. The base of the specimen rests on a one-way ball-bearing "sled", which allows for free lateral translation of the lower part of the specimen. For dilative sands (sands of high bulk density and tested under relatively low confining stress), while several conjugate shear bands typically form at peak stress, subtle material irregularities tend to favor the domination of one band [19,20]. If lateral translation between the regions above and below the dominant shear band is allowed, a single, persistent, minimally constrained and quasi-linear shear band will dominate; otherwise, the shear band may be biased by boundary constraints, e.g. it may be curved or multiple shear bands may ensue (e.g. [21]). The translatable lower boundary in our apparatus permits the required offset, leading to a single, persistent, nominally linear shear band [17]. The latex confining membrane is sufficiently flexible to permit around 100–150 % shear strain across a shear band.

To produce material color variation required for DIC use, we mixed two mined construction sands: Masonry sand, used for brick mason mortar, and concrete sand, used as aggregate in concrete mixes. To provide for a uniform grain size distribution, each sand was pre-sieved between the No. 16 and No. 30 US Standard sieves, resulting in a median grain size of around 0.84 mm and grain sizes ranging between 0.6 and 1.18 mm. The sands were then mixed in the ratio 90 % masonry, 10 % concrete by mass. The resulting sand, called "MC sand", was sub-rounded to sub-angular: micrographs of typical grains are shown in Fig. 2.

Test specimens are formed by raining sand from a 6-holed outlet device sized slightly smaller than the specimen cross-sectional area. A screen located about 0.5 cm below the outlet holes scatters the sand to encourage uniform distribution across the specimen cross section. The drop height was maintained constant at 12 cm throughout specimen formation, to ensure material uniformity versus height and to create dense

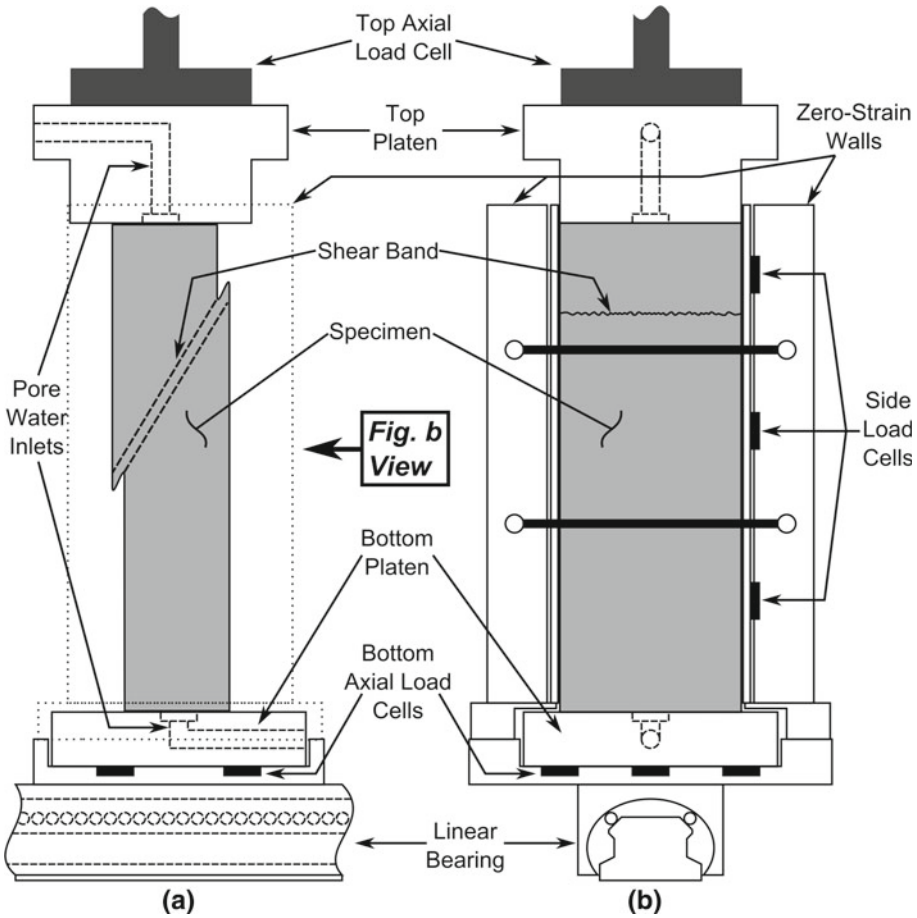

Fig. 1 Schematic of plane strain test specimen: **a** camera view, **b** out-of-plane specimen face

specimens that would be conducive to shear band formation. For the specimen discussed below, the bulk porosity was 0.36, corresponding to close to 100 % of the sand's bulk relative density.

After sand deposition, the specimen is confined under 40 kPa vacuum pressure, the forming mold is removed, and the specimen is placed inside the test frame. Then, the zero strain walls are anchored in place. A 41-cm-diameter acrylic cell is lowered over the specimen and sealed. The cell is filled with 10 cSt clear silicon fluid, which is then pressurized to 40 kPa while the vacuum pressure is simultaneously reduced.

Macroscopic specimen volume change is conventionally monitored by measuring the amount of pore water exchange to/from the specimen, and accurate measurements require 100 % pore saturation. To achieve this, de-ionized tap water is first percolated at low velocity through the specimen from bottom to top. The water is then pressurized with "back pressure". The back pressure, u, is increased incrementally until 100 % saturation is achieved, as determined by the B-value check [22]. The saturated specimen is then consolidated anisotropically (a non-zero initial shear stress is used to promote earlier shear band formation). Finally, drained, plane strain compression is performed by increasing the axial deformation, applied by a brushless servo motor, at a constant rate of 2 % axial strain (approximately 2.8 mm) per hour. A small displacement rate is used to avoid pore fluid pressure changes within the narrow shear band region.

Seven displacement transducers (not shown in Fig. 1) are positioned around the specimen to monitor macroscopic axial, lateral (in plane) and sled displacement, and to track the reduced cross sectional area caused by shear band offset (Fig. 1a) needed in axial stress calculations. Seven load cells (Fig. 1) collectively measure macroscopic axial and out of plane forces and frictional losses along the glass walls (coefficients of friction are typically 1–6°). Global specimen volumetric strain is monitored using a differential pressure transducer. Throughout shear, all sensor readings are recorded in 30-second intervals (every 0.0167 % axial strain). Data is recorded using a 16-bit resolution data acquisition (DAQ) system. Prior to sampling, each signal is run through a 10 Hz low pass digital filter to minimize in-line noise. The deviator stress invariant, q, is used to characterize global shear stress response:

$$q = \frac{1}{\sqrt{2}}\left[\left(\sigma_1' - \sigma_2'\right)^2 + \left(\sigma_1' - \sigma_3'\right)^2 + \left(\sigma_2' - \sigma_3'\right)^2\right]^{1/2} \quad (1)$$

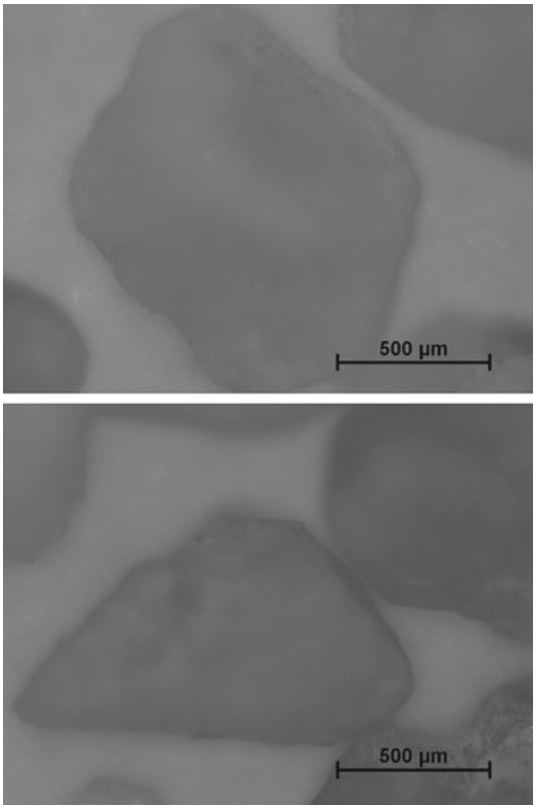

Fig. 2 Typical MC sand grains

In Eq. (1), the σ' indicate effective stresses, which represent the difference between the applied stresses, σ, and the pore water pressure, u.

Throughout shear, 5-Megapixel digital images of in plane specimen deformation are collected every 0.05 % axial strain (every 90 s) with a Point Grey Grasshopper camera. Figure 3 shows a 70 by 70 pixel portion of a typical image. Image scales are around 0.05 mm/pixel, so an average 0.84-mm sand grain is around 14 pixels across.

Figure 4 shows the global shear stress versus axial strain response of the dense MC sand specimen discussed below (the data points reference analysis increments discussed later). The specimen was consolidated to a mean normal effective stress ($p' = \sigma'_1 + \sigma'_2 + \sigma'_3$) of 290 kPa. The response is typical of dilative sands. The shear band is fully formed shortly after peak stress. At large strains, the specimen reaches the critical state, i.e. continuous shearing at constant stress (the volumetric strain in this test was biased by a leak; however, in other of our tests in this apparatus on the same or similar sands, constant volume was also exhibited at large strains (e.g., [18,23]).

2.2 Digital image correlation (DIC)

Digital image correlation (DIC) is a non-contact experimental technique to measure surface displacements on a deforming solid. Image correlation-based techniques such as DIC (mainly used in solids) and Particle Image Velocimetry, or PIV (aimed at individual particle tracking) have gained widespread acceptance in the experimental mechanics community for highly accurate, non-invasive subscale displacement measurement. DIC capitalizes on color variations on an object's surface (produced here by the multi-colored sand grains) by mapping gray level patterns within pixel subsets (e.g., Fig. 3) between two digital images depicting a deformation process. While a brief description of DIC is given below, more detail can be found in [24,25]. Other works by

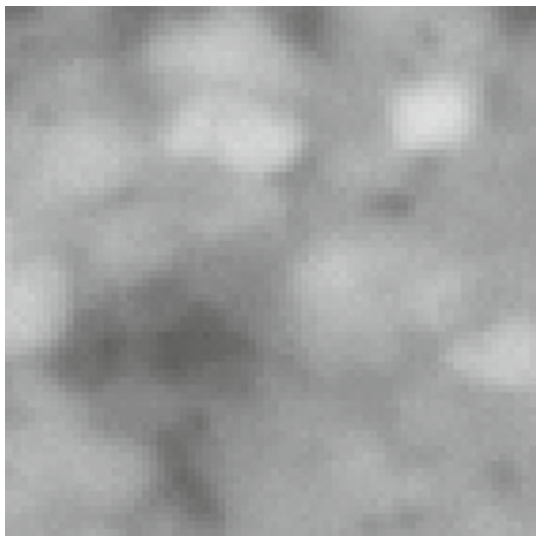

Fig. 3 70×70 pixel region from a typical digital image of an MC sand specimen during shear

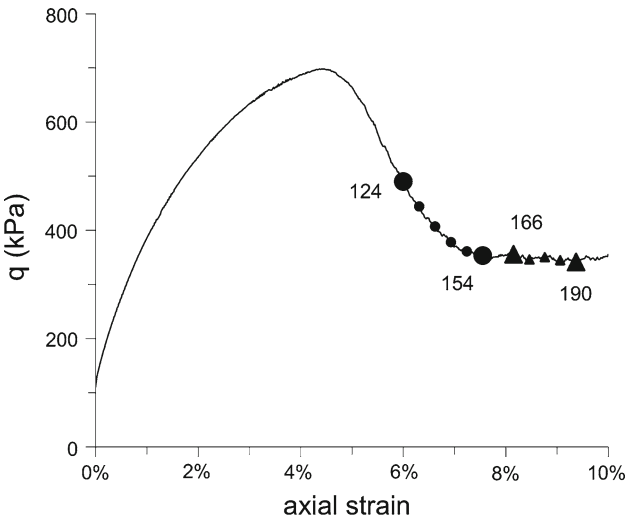

Fig. 4 Macroscopic shear stress versus axial strain response for dense MC sand in plane strain compression. *Circles* denote analysis increments in Fig. 7; *triangles* denote increments in Fig. 10. First and last image numbers for each respective sequence are labeled for clarity

the authors [18,26], discuss considerations specific to DIC use in dense granular solids.

The software VIC-2D by Correlated Solutions, Inc. was used to execute the DIC analyses. A pair of digital images reflecting a strain increment of interest is selected, and the target area for displacement measurement is divided into overlapping, initially square pixel subsets. Here, subsets were sized 63 pixels (slightly smaller than Fig. 3): this encompasses the equivalent of about four-by-four sand grains, manifests unique gray level patterns for reliable mapping, and is slightly smaller than the shear band thickness to enable discernment of individual vortices confined to within the shear band [26]. Subsets were spaced center-to-center 13 pixels, or about 0.75 mm, yielding displacement data point spacing on the order of a sand grain.

A subset is tracked between two images by minimizing a zero-normalized sum of squared differences (ZNSSD) error measure. To enable subpixel displacement resolution, the image gray level values are first interpolated to cubic order. To further improve mapping accuracy, subsets are allowed to deform to first order (note, the pixels themselves are not physically deforming; rather, the cubic-order continuous fit to the gray level intensities is deforming). Previous research [26] has shown that DIC analysis increments used here (0.1 % axial strain or about 3 % gross shear strain across the shear band) are sufficient to accommodate first order subset deformation. However, as will be seen below, correlated grain motion such as in vortex cells occurs over longer time/strain increments than afforded by the DIC analyses. To monitor displacements over longer strain increments, incremental DIC analyses are accumulated using the methodology described by Chupin et al. [27]. DIC displacement measurement accuracy for our apparatus, materials and analysis increments is around ±0.002 mm.

Figure 5 shows a portion of a typical DIC result, centered around the shear band. The results represent local displacements over a 0.3 % axial strain increment, from 6.5 to 6.8 % axial strain (Fig. 4). Note a larger strain increment is used here to more clearly illustrate the nature of the macroscopic deformation field. Displacement vectors for only 4 % of the DIC data points are shown for clarity. Axes indicate physical position along the specimen in the camera (x, y) reference frame (in subsequent discussions, the coordinate axis frame will be rotated to align with the shear band). The material above the shear band is seen to be translating vertically downward with the prescribed axial displacement, the material below the shear band is translating horizontally with the base sled, and all significant specimen deformation is confined to within the shear band (that the shear deformation field appears non-symmetric about the shear band centerline results from the kinematic perspective of both the top and bottom of the shear band moving at angles oblique to the shear band axis).

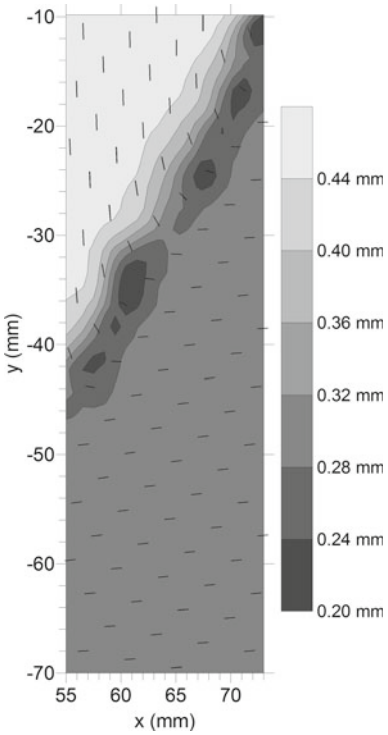

Fig. 5 Typical DIC result: displacement norm

3 Residual displacements

To pursue detection and characterization of vortex structures and their evolution, we examine fluctuations from the mean shear displacement field by analyzing residual displacements (e.g. [9]). Figure 6a shows vectors of the true specimen displacements centered around the shear band, plotted in the shear band reference frame (x*, y*), wherein the x*-axis is parallel to and the y*-axis perpendicular to the shear band axis. Axes indicate physical position along the shear band in millimeters. The displacements represent the accumulated axial strain increment 6.5–7.1 % (Fig. 4), which approximately represents the softening-critical state transition. Figure 6b shows the adjusted displacements after the base sled movements are subtracted. Vector lengths in Fig. 6a, b are scaled relative to the maximum and minimum values in both plots. The shear band boundaries are delineated by thresholding the displacement gradient, since only the material within the shear band is subject to significant non-zero strain (Fig. 5). Recall, however, that the DIC technique tracks the collective behavior of small clusters of grains, here about 4 grains across. Each DIC data point thus reflects the average displacement of the cluster, marked at the cluster's center. Thus, due to this local averaging, the DIC technique will manifest a gradual transition into and out of the shear band, rather than a discrete behavioral transition. We thus choose a displacement gradient threshold slightly higher than that

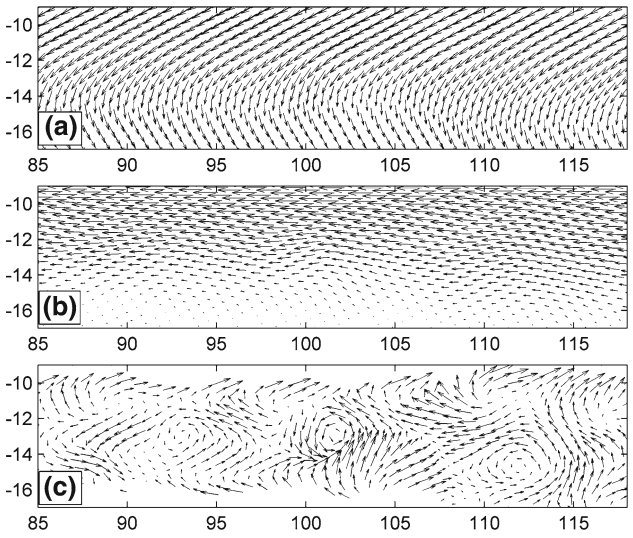

Fig. 6 Residual displacement determination shown in shear band coordinates: **a** true displacements; **b** displacements adjusted to stationary base sled; **c** residual displacements (superimposed affine field subtracted from **b**)

above the DIC noise, so as to filter out behavior in the transitional area near the shear band boundary.

Once the shear band boundaries are delineated, a mean shear field is fit across the determined boundaries and subtracted from the observed displacements. The resulting residual displacements are shown in Fig. 6c. Vectors are scaled according to the maximum and minimum residual displacements. Note that due to the discrete nature of granular media, the shear band boundary is nonlinear both in time and space (at any instant, a grain may be pulled into or moved out of the shear band), and this gives the shear band a locally undulating character.

Over the section of shear band shown in Fig. 6c, three distinct, co-rotating, vortices are clearly seen (centered approximately at x* locations of 93, 102 and 112 mm). The vortex centers correlate with the peaks in rotational strain seen previously by the authors [17,18]. At the conflux between adjacent vortices, the residual displacements are in opposition and induce local volumetric contraction [26]. Interestingly, we do not see evidence of "microbands" of slip between adjacent vortices, as were seen by Alonso-Marroquin et al. [8] and Tordesillas et al. [15] in simulations on circular particles. This difference suggests that for more angular grains, such as ours, grain slip is not a primary mode of dissipation, as it is likely inhibited due to geometric interlocking among the irregularly shaped particles.

A further observation in Fig. 6c is the presence of opposite-trending, rotational "wakes" near the shear band boundaries, typically located in between the main vortices. As will be seen below, these "wakes" seem to derive from the main vortices. While opposite direction particle slip and/or rotation has been detected in experiments [5] and simulations [28], coordinated grain motion, in particular in the form of counter-rotating wakes as seen in Fig. 6c, was not reported.

4 Evolution of vortex structures

We now examine the temporal patterning of vortex formation, dissolution, and reformation throughout post-peak deformation. While data from only one test is shown, we emphasize that the behavior and general patterns of response are consistent among all of our tests analyzed to date. Figure 7 presents residual displacements for five consecutive strain increments (between the filled circles in Fig. 4) comprising softening, the softening-critical state transition, and the initial stages of critical state. The sense of shear is the top of the band moving left, bottom of the band stationary. Each plot represents behavior over a 0.3 % axial strain increment, or about 9 % gross shear band shear strain, determined by accumulating three 0.1 % incremental DIC analyses. We reference each residual displacement increment in Fig. 7 to the image numbers bounding the increment. As images were collected every 0.05 % axial strain, the increment spacing is six image numbers: so, for example, the first increment represents displacements between images 124 and 130 (first two data points in Fig. 4); the second increment represents displacements between images 130 and 136 (second two data points in Fig. 4); and so on. Only the first and last image numbers, 124 and 154 are labeled in Fig. 4 for clarity. All plots are referenced to the base sled position corresponding to image 124: so, from one increment to the next, the top of the shear band translates leftward about 0.5 mm. Because shearing rate is constant, if velocity fluctuations were desired, then displacement magnitudes would simply be divided by a constant time. We additionally note that the strain increments chosen for analysis in Fig. 7 were arrived upon after much trial and error. While they may not represent the durations of all kinematic entities precisely, they were found to most optimally reveal vortex presence and lifetime, which is our interest here.

The first increment in Fig. 7, between image numbers 124–130, represents behavior entirely during softening. The specimen is still macroscopically dilating, e.g. [18,23]; and, since this dilation is confined to the shear band, shear band thickness is thus increasing, yielding predominantly upward-oriented residual displacements. The horizontal components of residual displacement along the shear band length are fluctuating in magnitude and are generally non-affine of the form shown in Fig. 8. Note that if deformations were affine, the horizontal components of the residual displacements would be zero. Several zones of affine-like deformation are seen and are shaded (green online) in Fig. 7. We argue that these regions indicate potential locations of semi-stable

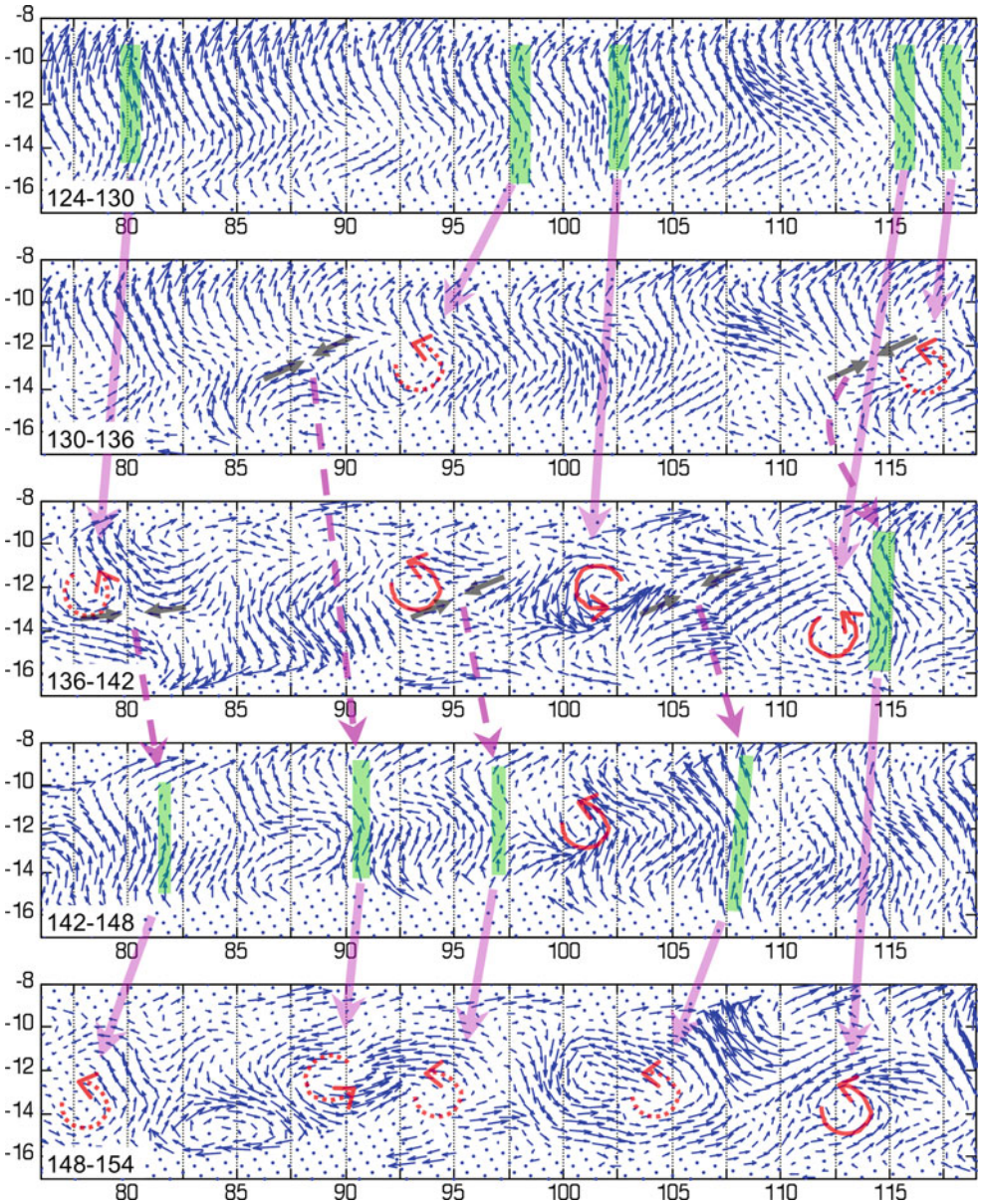

Fig. 7 Residual displacements over the sequence of strain increments indicated by circle data points on Fig. 4. Sense of shear is top moving left. Zones of affine deformation indicated by wide *vertical lines* (*green online*). Vortices indicated by thick CCW *arrows* (*red online*). *Dotted arrows* (*red online*) indicate pre-formed vortices or vortex-like structures. Thick gray opposing *arrows* indicate regions of grain jamming

force chains, as schematically demonstrated in Fig. 9: if particle mobilization is associated with force chain destabilization [14], a lack of inter-particle motion can signify existence of stable force chains. While this association is certainly not exclusive (contacts can be immobile among non-force chain particles as well), it provides a starting point for identifying plausible kinematic signatures of potentially stable force chains amidst our data.

In the following increment, 130–136, we see no evidence of affine deformation anywhere along the shear band length. Partially formed vortex-like structures have been induced at x*=93 and 117 mm, just ahead of two of the affine deformation zones from the previous increment. The rightmost of these rotational entities is arrested from full vortex formation, due to opposing displacements from the vortex forming immediately to its left. Such "jamming", where displacements are in opposition and relative motion is stalled, is also seen ahead of the middle-left vortex; but in this case, the jamming is spatially distanced from the vortex to the extent that it does not inhibit the vortex from full formation (see increment 136–142).

By the next increment, 136–142, three fully circulating vortices have formed at x*=93, 102, and 112 mm, spatially just ahead of the affine zones identified in increment

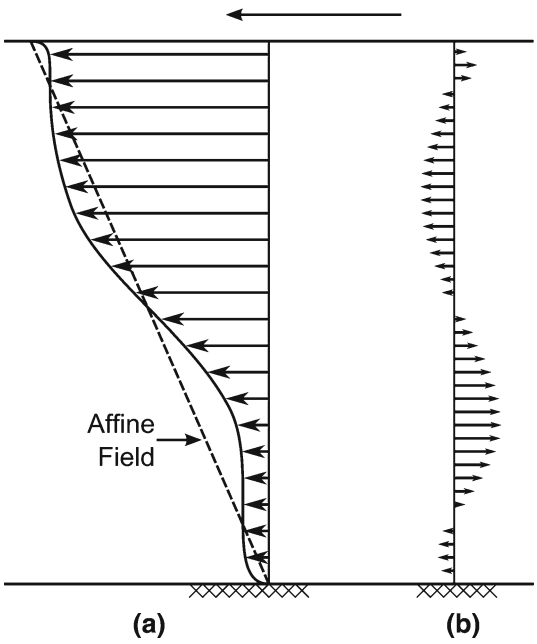

Fig. 8 Conceptual depiction of the character of along-band-components of shear band displacements (**a**) and their ensuing residual displacements (**b**)

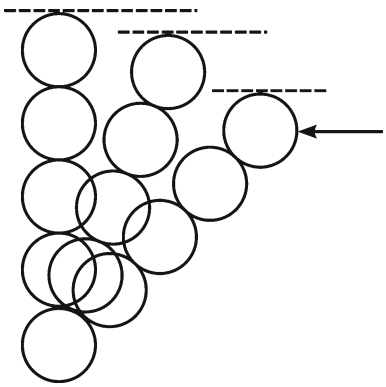

Fig. 9 Schematic representation of affine deformation of a stable force chain with a fixed base and sheared leftward. *Dotted line* represents upper shear band boundary

124–130. Williams and Rege [10] hypothesized that their circulation cells were initiated by force chain buckling, and the data in Fig. 7 strongly suggest this mechanism has occurred here (note that an additional vortex has been induced at x* = 78, ahead of the leftmost affine zone of increment 124–130; however, it is inhibited from fully forming due to surrounding displacement opposition and corresponding jamming). Further, this increment, 136–142, also approximately represents the softening-critical state transition: the rate of softening has significantly decreased (Fig. 4), and macroscopic volumetric dilation has largely ceased (while macroscopic volumetric data is not shown here, we affirm the cessation of volumetric dilation at this point based on previous research [17,18,23]). We thus augment our previous microstructural interpretation of the softening-critical state transition [18]: the softening-critical state transition is microstructurally defined by a coordinated, multi-force chain collapse event that induces vortex-like structures born out of collapsing force chains.

We additionally see in increment 136–142 local jamming between adjacent vortices. This jamming induces local volumetric contraction [26], but also serves to arrest the vortices from further progress: in the following increment, 142–148, only one vortex remains. Further, regions of affine-like deformation have formed directly behind the jammed regions of previous increments. These results suggest that jammed regions become target locations for the birth of potential new force chains: indeed, jamming has been linked (e.g. [14]) to force chains (and, by inference, to stable inter-particle contacts). As shear stress is nearly constant (Fig. 4), we argue that this point in the sequence marks the transition into the critical state of deformation. In the final increment of the sequence, 148–154, we see that ahead of each zone of affine deformation from the previous increment, a new vortex or vortex-like structure has formed (three of the five vortices cannot form due to jamming from other vortex activity in close proximity).

To demonstrate that the sequence seen in Fig. 7 is ongoing, we continue in Fig. 10 with the sequence of incremental behavior between images 166 and 190 (triangles in Fig. 4), which entirely represents critical state deformation. The first two increments, 166–172 and 172–178, are predominantly characterized by vortex-like activity and jamming (one zone of affine deformation is still evident in 166–172, but an ensuing vortex is formed in front of it by 172–178). Note, however, that none of the vortices were able to achieve full formation due to close proximity of the vortices and associated local jamming. In the third increment, 178–184, the residual displacements again manifest significant upward components, similar to that seen in increment 142–148 (Fig. 7). And again, several regions of affine-like deformation can be identified, which in all cases have formed behind previously jammed regions. In the final increment, 184–190, new vortices or partially formed vortex-like structures have formed, each directly ahead of the affine zones from the previous increment. The affine zone at x* = 101 mm in increment 178–184 does not yield a coherent vortex in increment 184–190, as it has been obstructed due to opposing displacements from an adjacent vortex.

To summarize, the coordinated, multi-force chain collapse event defining the softening-critical state transition induces the formation of co-rotating vortices. Local jamming at the conflux of opposing displacements between adjacent vortices then arrests vortex motion. This then marks the transition into the critical state of deformation, which is microstructurally defined by a temporally recurring pattern of: (a) force chain

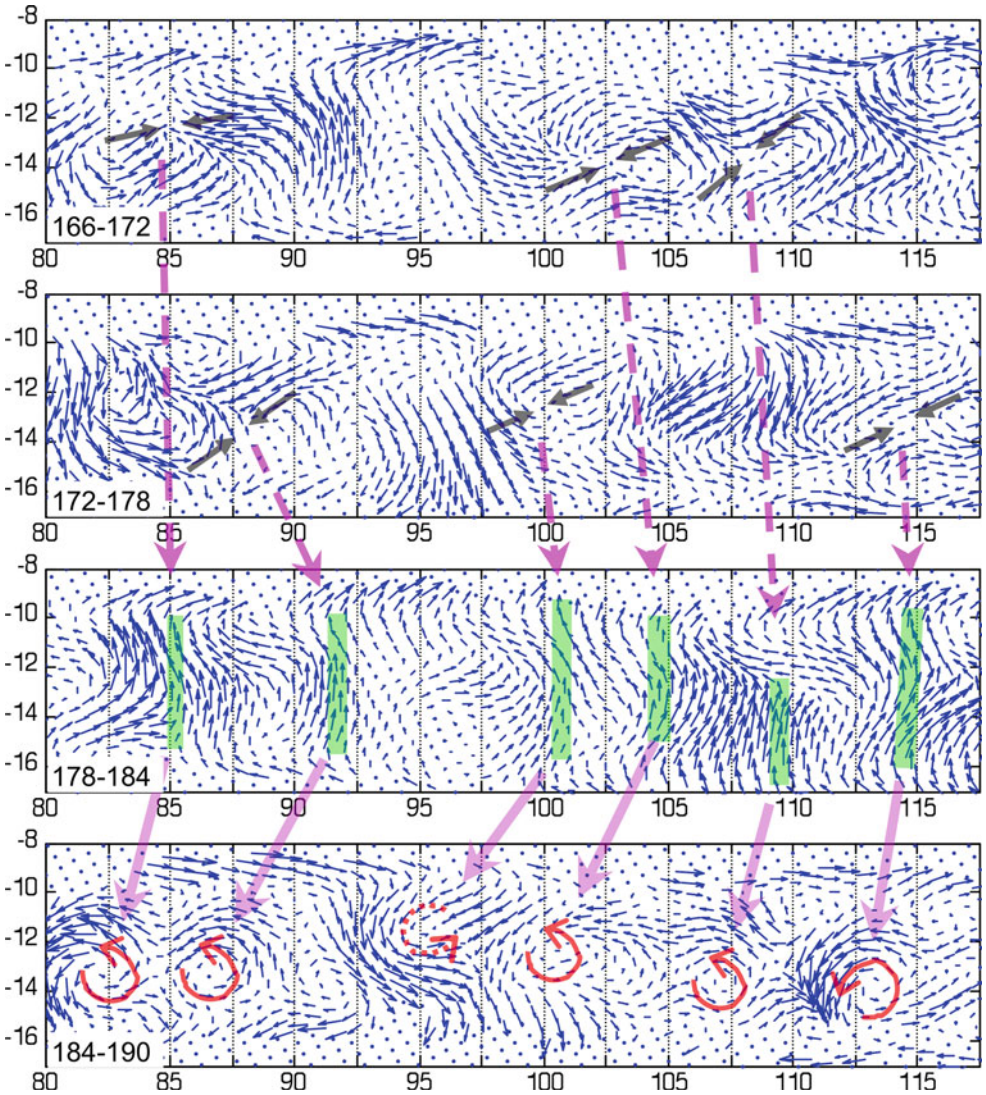

Fig. 10 Residual displacements during critical state over the sequence of strain increments indicated by triangle data points on Fig. 4. Sense of shear is *top* moving *left*. Zones of affine deformation indicated by wide vertical (*green online*) lines. Vortices indicated by thick CCW *arrows* (*red online*). *Dotted arrows* indicate pre-formed vortices or vortex-like structures. Opposing arrows indicate regions of grain jamming

birth at or behind regions of local jamming, (b) force chain collapse and the induction of new, co-rotating vortices ahead of the collapsing force chains, and (c) jamming at the conflux of opposing displacements between adjacent vortices. The pattern is temporally recurring, and indeed not spontaneous. Vortices are relatively short lived: here, we saw their temporal lifetimes were typically around 9 % shear strain, and in one case were evidenced for 18 % shear strain ($x^* = 101$–102 mm in increments 136–142 and 142–148, Fig. 7). We further note that the counter-rotating "wakes" mentioned in Fig. 6 were only present in increments where vortices were present. This observation reinforces our hypothesis that these wakes are generated by the vortices themselves, and may be a necessary deformation mechanism to fuel vortex coherency.

5 Influence of microstructure on macroscopic response

The microstructural behavior seen in Figs. 7 and 10 was further seen to correlate with macroscopic response. In Fig. 11, we zoom in on the macroscopic shear stress response as a function of axial strain (Fig. 4) between images 130 and 190. We delineate on this graph the predominant types of meso-scale behavior that were seen in each increment of Figs. 7 and 10: "A" indicates affine-like deformation, "V" indicates vortices, and "J" indicates jamming. Note that the minor fluctuations in the shear stress response in Fig. 11 are in part due to slight fluctuations in the cell confining pressure, due to the finite resolution of the controlling transducer. However, apart from that, during critical state (starting just before image 148), we see two

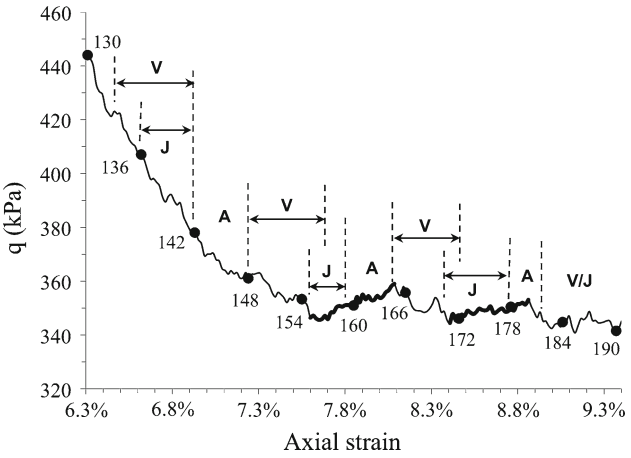

Fig. 11 Prominent meso-scale kinematics as a function of macroscopic stress-strain response: *A* affine-like deformation, *J* jamming, *V* vortices. *Thicker lines* emphasize stress rises during critical state

sections of relative stress rise (shaded in bold). In both cases, the stress rises correlate with microstructural jamming and affine deformation. Further, the subsequent stress drops were both associated with vortex formation. Note that the stress drops for our real sands tend to be gradual, compared to the more dramatic stress drops often associated with circular particles (e.g. [8]). Alonso-Marroquin et al. [8] attributed observed reductions in friction coefficient with the formation of rolling bearings. Here, we see that the reductions in shearing resistance correlate with coordinated grain motion in the form of vortices.

The influence of the evolving microstructure on macroscopic response during softening (increments prior to image 148) is subtler, as macroscopic shear stress is decreasing throughout (Fig. 4). While not shown here, in increments prior to 124–136 (Fig. 7), no jamming or fully formed vortices were seen. However, in increments 136–142 and 142–148, which are marked by jamming and affine-like deformation, respectively, we see macroscopic response evolve from decreasing shear stress to shearing at nearly constant stress. Thus, it can be said that jamming and force chain formation have served to completely arrest softening: by image 148, shear stress is roughly constant.

In Figs. 7 and 10, we see little evidence of "microbands" of slip deformation in between adjacent co-rotating vortices [8,15]. Due to the averaging nature of the DIC technique described above, microbands, 1–4 particle diameters wide [11], would here be evidenced by a gradual transition of parallel displacement vectors to opposite orientations over a limited spatial area [26]. In only one case did we see meso-scale displacements of this character: in Fig. 7, increment 136–142, x* = 81 mm. The far more common observation in our data were converging displacements, e.g. Fig. 6c, x* = 108 mm. Thus, for sands with non-spherical, irregular shaped grains, frictional slip seems to be inhibited, likely by particle interlocking. The more gradual stress reductions we see in Fig. 11 (in contrast to the significant stress drops associated with circular particles, e.g. [8]) further emphasize the lack of slip evidenced in our sub-angular sands.

We again emphasize that the behavioral trends seen in Figs. 7, 10 and 11 were seen in all our tests, conducted on two uniform sands of two different median grain sizes. We also have seen the same trends in experiments conducted on bidisperse mixtures of glass beads (the effects both of grain shape and size are reserved for a separate discussion). In all cases, the temporal sequences of mesoscale displacement fluctuations were consistent. The spatial variation in response along the shear band, in some cases, caused the effect on macroscopic response to be more subtle in some increments versus others: for example, when only one vortex was seen, the stress drops tended to be more subtle than when several vortices were seen. However, in no case did a stress drop occur with no evidence of vortex-like behavior along the shear band. Similarly, in no case was a stress rise seen without jamming and affine-like deformation evidenced along the band. This consistent correlation among macroscopic response and mesoscale behavior is particularly encouraging, as it suggests that the behavior we are observing along the surface of our specimens is consistent with behavior within the shear band depth.

6 Conclusions

Digital image Correlation (DIC) has been used to quantitatively measure grain scale displacements in shear bands in dense sands undergoing plane strain compression. We have observed a systematic and temporally recurring pattern of vortex formation, dissolution, and reformation within the shear band throughout critical state. During softening, deformation along a shear band is largely non-affine, although several zones of affine-like deformation are evidenced and are argued to be indicative of semi-stable force chains. At the softening-critical state transition, a coordinated multi-force chain collapse event triggers the formation of co-rotating vortices. At the onset of critical state, jamming at the confluence of opposing displacements between adjacent vortices arrests further vortex evolution, and local volumetric contraction in these jammed zones leads to the formation of new zones of affine deformation. We propose that these affine zones are indicative of new force chain birth. The critical state of deformation is then characterized microstructurally by a repeating temporal sequence of force chain collapse, vortex induction, jamming, vortex dissolution, and potential new force chain formation. The temporal changes in meso-scale kinematics are seen to additionally correlate with fluctuations in macroscopic shear stress: vortex formation is associated with stress reductions, whereas jamming and affine deformation

tie in with temporary rehardening. The stress drops and rises were gradual, rather than abrupt, suggesting that grain-grain slippage is not a prominent mechanism of dissipation in our angular sands. That we also see little evidence of microband slip between co-rotating vortices strengthens this observation.

Acknowledgments The authors sincerely thank the US National Science Foundation (grant CMMI-0748284), the University of Southern California, and the University of Southern California Women in Science and Engineering (WiSE) Program for their financial support of this research. We would also like to acknowledge the anonymous reviewers, whose keen comments and advice have helped to strengthen the manuscript.

References

1. Drescher, A., De-Josselin-de-Jong, G.: Photoelastic verification of a mechanical model for the flow of a granular material. J. Mech. Phys. Solids. **20**(5), 337–351 (1972)
2. Majmudar, T.S., Behringer, R.P.: Contact force measurements and stress-induced anisotropy in granular materials. Nature **435**(7045), 1079–1082 (2005)
3. Tordesillas, A., Muthuswamy, M.: On the modeling of confined buckling of force chains. J. Mech. Phys. Solids. **57**(4), 706–727 (2009)
4. Bardet, J.P., Proubet, J.: Numerical investigation of the structure of persistent shear bands in granular media. Geotechnique **41**(4), 599–613 (1991)
5. Veje, C.T., Howell, D.W., Behringer, R.P.: Kinematics of a two-dimensional granular Couette experiment at the transition to shearing. Phys. Rev. E. **59**(1), 739–745 (1999)
6. Oda, M., Iwashita, K.: Study on couple stress and shear band development in granular media based on numerical simulation analyses. Int. J. Eng. Sci. **38**(15), 1713–1740 (2000)
7. Rognon, P., Einav, I.: Thermal transients and convective particle motion in dense granular materials. Phys. Rev. Lett. **105**(21), 218301 (2010)
8. Alonso-Marroquín, F., Vardoulakis, I., Herrmann, H.J.: Effect of rolling on dissipation in fault gouges. Phys. Rev. E. **74**(3), 031306 (2006)
9. Williams, J.R., Rege, N.: Coherent vortex structures in deforming granular materials. Mech. Coh. Fric. Mat. **2**(3), 223–236 (1997)
10. Williams, J.R., Rege, N.: The development of circulation cell structures in granular materials undergoing compression. Powder Technol. **90**(3), 187–194 (1997)
11. Kuhn, M.R.: Structured deformation in granular materials. Mech. Mater. **31**(6), 407–429 (1999)
12. Radjai, F., Roux, S.: Turbulentlike fluctuations in quasistatic flow of granular media. Phys. Rev. Lett. **89**(6), 064302 (2002)
13. Thornton, C., Zhang, L.: A numerical examination of shear banding and simple shear non-coaxial flow rules. Philos. Mag. **86**(21–22), 3425–3452 (2006)
14. Tordesillas, A.: Force chain buckling, unjamming transitions and shear banding in dense granular assemblies. Philos. Mag. **87**(32), 4987–5016 (2007)
15. Tordesillas, A., Muthuswamy, M., Walsh, S.D.C.: Mesoscale measures of nonaffine deformation in dense granular assemblies. J. Eng. Mech. **134**(12), 1095–1113 (2008)
16. Utter, B., Behringer, R.P.: Self-diffusion in dense granular shear. Flows. Phys. Rev. E. **69**(3), 031308-1–031308-12 (2004)
17. Rechenmacher, A.L.: Grain-scale processes governing shear band initiation and evolution in sands. J. Mech. Phys. Solids. **54**(1), 22–45 (2006)
18. Rechenmacher, A.L., Abedi, S., Chupin, O.: Evolution of force chains in shear bands in sands. Geotechnique **60**(5), 343 (2010)
19. Gudehus, G., Nubel, K.: Evolution of shear bands in sand. Geotechnique **54**(3), 187–201 (2004)
20. Borja, R.I., Andrade, J.E.: Critical state plasticity. Part VI: meso-scale finite element simulation of strain localization in discrete granular materials. Comput. Methods Appl. Mech. Eng. **195**(37–40), 5115–5140 (2006)
21. Desrues, J., Viggiani, G.: Strain localization in sand: an overview of the experimental results obtained in Grenoble using stereophotogrammetry. Int. J. Numer. Anal. Methods Geomech. **28**(4), 279–321 (2004)
22. Head, K.H.: Manual of Soil Laboratory Testing. Volume 3: Effective Stress Tests. Wiley, West Sussex (1998)
23. Finno, R.J., Rechenmacher, A.L.: Effects of consolidation history on critical state of sand. J. Geotech. Geoenv. Eng. **129**(4), 350–360 (2003)
24. Sutton, M.D., McNeill, S.R., Helm, J.D., Chao, Y.J.: Advances in two-dimensional and three-dimensional computer vision. In: Rastogi, P.K. (ed.) Photomechanics: topics in applied physics, pp. 323–372. Springer, Berlin (2000)
25. Sutton, M.A., Orteu, J.-J., Schreier, H.W.: Image Correlation for Shape, Motion and Deformation Measurements. Springer, New York (2009)
26. Rechenmacher, A.L., Abedi, S., Chupin, O.: Characterization of mesoscale instabilities in localized granular shear using digital image correlation. Acta Geotech. **6**(4), 205–217 (2011)
27. Chupin, O., Rechenmacher, A.L., Abedi, S.: Finite strain analysis of nonuniform deformation inside shear bands in sands. Int. J. Numer. Anal. Methods Geomech. (2011). doi:10.1002/nag.1071
28. Hu, N., Molinari, J.F.: Shear bands in dense metallic granular materials. J. Mech. Phys. Solids. **52**(3), 499–531 (2004)